Impact-velocity dependence of ejected-electron distributions for ionization in proton-hydrogen collisions

Emil Y. Sidky and C. D. Lin

Department of Physics, Cardwell Hall, Kansas State University, Manhattan, Kansas 66506

(Received 26 February 1999)

Ab initio calculations of ejected-electron momentum distributions are presented for proton on hydrogen collisions at impact energies ranging from 5 to 100 keV and an impact parameter of 1.2 a.u. At low energies the transverse momentum distributions show a double-peak structure similar to what is predicted by a two-state Sturmian theory [Macek and Ovchinnikov, Phys. Rev. Lett. **80**, 2298 (1998)]. In contrast to that theory, however, we do not find the rapid oscillations in the transverse momentum distribution for impact energies between 5 and 15 keV. At higher collision energies the double-peak transverse momentum distribution coalesces into a single peak. For the energy range considered, the longitudinal momentum distribution shows a broad peak at half the projectile velocity except at the higher energies where the distribution moves toward the target nucleus. [S1050-2947(99)08807-1]

PACS number(s): 34.10.+x

I. INTRODUCTION

In recent years much attention has been given to establishing the angular and energy distributions of the ejected electrons in ion-atom collisions in an attempt to understand the detailed mechanisms of the ionization process. One controversial point has been the role of saddle-point electrons [1] which attain escape energy by riding the saddle located at the center of charge. Early experiments, which measured the energy distributions of the electrons for proton collisions with helium atoms in the energy range of tens to hundreds of keV, drew conflicting conclusions [2–11]. The controversy regarding the saddle-point electrons involved ion-atom collisions where the projectile velocity was above the ''matching'' velocity, the average speed of the target's valence electron. Early quantum mechanical calculations [12] and later ones [13–15] based on the triple-centered close-coupling approximation revealed the importance of describing the electron probability near the saddle point in the calculation of total ionization cross sections for ion-atom collisions involving projectiles moving below the matching velocity. Hidden crossing theory [16] also predicts that saddle-point electrons comprise a large fraction of the total ionization cross section. However, none of these theories provide a quantitative description of the complete velocity distribution of ejected electrons. The first experiment, which measured the energy distribution of ejected electrons for proton-hydrogen collisions, was performed by Pieksma *et al.* [17]. It too left the ionization mechanism in ion-atom collisions to debate. It too did not resolve the role of saddle-point electrons in the ionization mechanism unambiguously.

In recent years, the novel technique of cold target recoil-ion momentum spectroscopy (COLTRIMS) allows experimentalists to map out the full momentum distributions of the ejected electrons. COLTRIMS experiments obtain essentially complete quantum mechanical information for ionization processes, providing a stringent test for theory. For protons colliding with helium atoms in the 5–15 keV region, data from Dörner *et al.* [18] show momentum distributions of the electron split into two jets pointing on either side of the projectile velocity in the collision plane. The size of the

two peaks alternates rapidly with respect to the collision energies from 5 to 15 keV. Subsequently, more experiments have been done on ionization of a He or Ne target with different projectiles [19–21], and the ejected-electron momentum distributions appear to depend strongly on the system studied.

According to the molecular promotion model for ion-atom collisions, excitation and ionization at low energies occur via a series of avoided crossings where the electron is promoted to higher molecular potential curves. The observation of double-peak structure in the transverse electron momentum distribution implies that molecular π orbitals are populated in the ionization process. By extending the Born-Oppenheimer approximation through analytic continuation to the complex values of the internuclear distance, the ''hidden crossing'' theory recasts the mechanism of excitation and ionization at low energies via a series of branch points connecting the potential surfaces. The hidden crossing theory identifies two T series, the T_{00} and T_{01}, where the electron is promoted to the continuum near the saddle point of the p+H system. In a further extension, the Sturmian theory was developed with the aim of providing a full description of the ionization process, including the prediction of the momentum distribution of the ejected electron. Applying Sturmian theory to p+H collisions, the T_{00} promotion of the $1s\sigma$ and the T_{01} promotion of the $2p\pi$ states were carried out [22,23]. The electron momentum distribution obtained from the T_{00} promotion gives a single peak centered on the potential saddle and T_{01} promotion predicts the double-peak structure in the transverse direction, as one expects from π orbitals. To obtain the complete distribution of ionization near the saddle point, it was assumed that the T_{00} and T_{01} are the main contributors of saddle-point electrons. The phase between the two paths to ionization was calculated by Macek and Ovchinnikov [24], showing a strong dependence on projectile velocity, and thus the two peaks in the transverse momentum distribution exhibit rapid oscillations with collision energy. The rapid oscillation turns out to be identical to the oscillations seen by Dörner *et al.* [18] for proton on helium collisions at the same energies. This agreement is probably better attributed as coincidental, since there is no reason to

believe that the two systems should have identical momentum distributions for the ejected electrons at the same collision energies. Indeed, experimental results for other collision systems such as He^+ on He, He^{2+} on He, and He^+ on Ne [19–21] all show distinct momentum distributions. One would thus expect that mechanisms for ionization at low energies, like charge transfer or excitation processes, would depend on specific systems. In the meanwhile, the range of the validity of the two-state Sturmian theory is not clearly established. Thus it is desirable to compute the ejected-electron distribution in proton on hydrogen collisions using an *ab initio* approach.

To calculate the ejected-electron distribution in ion-atom collisions a complete representation of the continuum electron in the field of two moving Coulomb centers is necessary. To describe the electronic wave function within a finite basis, we choose to expand it in the momentum space since the range of the momentum is confined in a collision. In a previous article [25] we have developed the two-center momentum-space discretization (TCMSD) method to efficiently calculate the momentum-space electron wave function. Other work in solving the time-dependent Schrödinger equation for ion-atom collisions has been performed by direct solution on a lattice in momentum space [26] and in configuration space [27–29]. These large-scale grid calculations execute on supercomputers, since they do not take advantage of the basic two-center nature of the ion-atom collision and these calculations do not explore the momentum distributions of the ejected electron. In this article we briefly discuss TCMSD focusing on recent improvements which allow calculations for a wide range of projectile energies, extending from 5 to 100 keV and at an impact parameter of 1.2 a.u., where the contribution to ionization is maximal. A detailed analysis of the positive energy component of the total electron wave function is presented. Ejected-electron distributions in momentum space are shown as a function of projectile velocity.

II. THE THEORETICAL FRAMEWORK

The proton on hydrogen collision system is viewed in the standard semiclassical framework, where the internuclear motion is classical and the electron is treated fully quantum mechanically. Moreover, we assume rectilinear motion for the projectile center with constant velocity $\vec{v}$ and impact parameter $\vec{b}$. The time-dependent Schrödinger equation, written in the target frame, for an electron in the field of the two protons is

$$i\frac{\partial}{\partial t}\psi(\vec{r},t) = \left(-\frac{1}{2}\nabla^2 - \frac{1}{|\vec{r}|} - \frac{1}{|\vec{r}-\vec{R}|} \right)\psi(\vec{r},t), \quad \vec{R} = \vec{v}t + \vec{b}.$$
$$(1)$$

The coordinate system is the natural frame, where the projectile velocity $\vec{v}$ is along the x axis, the impact parameter is along the y axis, and the z axis is perpendicular to the collision plane. Atomic units are used throughout. The details on the two-center momentum-space descretization method, employed to solve Eq. (1), are presented in Ref. [25]. Here, we restate the form of the electronic momentum-space wave function, and give a brief account of how the time-dependent

wave function is found. We discuss how bound-state and ionization amplitudes are derived from the wave function. Finally, we discuss the calculational parameters necessary to solve Eq. (1) for protons on hydrogen with impact energy ranging from 5 to 100 keV at an impact parameter of 1.2 a.u.

A. Wave-function propagation

The electron wave function in the ion-atom collision is represented by a two-center expansion in momentum space:

$$\Phi(\vec{p},t) = \sum_{l,m} \tilde{T}_{l,m}(p,t)Y_{l,m}(\hat{p})$$

$$+ e^{-i[\vec{p}\cdot\vec{R}-(1/2)v^2t]}\sum_{l,m} \tilde{P}_{l,m}(q,t)Y_{l,m}(\hat{q}),$$

$$\vec{q} = \vec{p} - \vec{v} \qquad (2)$$

where the spherical harmonic $Y_{l,m}$ is defined with respect to each center in the momentum-space expansion and the phase factor in front of the second sum on the right is the plane-wave electron translation factor in the momentum space. We have carried out a partial wave expansion on each center and the radial functions, $\tilde{T}_{l,m}(p,t)$ and $\tilde{P}_{l,m}(q,t)$, are in turn expanded in B splines:

$$\tilde{T}_{l,m}(p,t) = \sum_{i=1}^{N-1} c_i^{lm}(t)\tilde{B}_i(p) + c_N^{lm}/p^{4+l}. \qquad (3)$$

Note that the high momentum part in the second term is proportional to the asymptotic form for each partial wave. The projectile radial functions have a similar expansion in q with the spline coefficients labeled d_i^{lm}. The present calculation is an improvement over Ref. [25] in that fourth-order B splines replace the previous second-order B splines, and the B-spline knot points can be varied for each harmonic individually, allowing more detailed representation of the harmonics that are expected to be important.

Substituting Eq. (2) into Eq. (1) gives a set of first-order coupled equations for the expansion coefficients in Eq. (3). The coefficients $c_i^{lm}(t)$ and $d_i^{lm}(t)$ are arrived at through a fourth-order fixed step-size Runge-Kutta integration. The time derivative of the B-spline coefficients at each integration step results from a least squares fit to $H\psi$ at a set of points which typically outnumber the basis functions by a factor of 4. The fit is performed in configuration space after inverse Fourier transformation of the basis functions, $\tilde{B}_i(p)Y_{l,m}(\hat{p})$ and $e^{-i[\vec{p}\cdot\vec{R}-(1/2)v^2t]}\tilde{B}_i(q)Y_{l,m}(\hat{q})$. The fitting points are arranged as a spherical polar grid about both target and projectile protons. The linear system solved is shown schematically:

$$[(A^T)_{K'J}A_{JK}]x_K = (A^T)_{K'J}b_J. \qquad (4)$$

Products with like indices imply summation. K and K' are indices running through all basis functions, and J is an index running through all the fitting points. The matrix A is a rectangular matrix of all basis functions evaluated at all fitting points. The least squares method prescribes multiplying through by A^T, providing a square linear system. The vector x_K represents the time derivative of the coefficients, and the

vector b_J represents $-iH\psi$ evaluated at the fitting points. The χ^2 of the fit reveals the error of the time derivative of the electron probability density. Once x_K is found this information is fed into the Runge-Kutta integration, which is checked for accuracy by the wave function normalization and by reducing the integration step size.

B. Wave function analysis

The numerical wave function, having passed the numerical checks, is analyzed to extract the bound-state amplitudes. We neglect overlaps between the two centers and perform bound-state projection individually on the target and projectile centers:

$$a_{nlm}^{T(P)}(t) = \int_0^\infty F_{nl}(p)\widetilde{T}(\widetilde{P})_{lm}(p,t)p^2 dp. \qquad (5)$$

Here F_{nl} is the hydrogenic radial function in momentum space. The amplitudes $a^{T(P)}(t)$ will, in general, oscillate as a function of time due to the omission of any overlap integrals, but they will eventually reach the asymptotically correct value as the overlap between the target and projectile centers must go to zero for bound states. As with other methods, which integrate the Schrödinger equation for the total wave function (see, for example, Ref. [27]), ionization is calculated by subtracting away the bound component:

$$\widetilde{T}(\widetilde{P})_{lm}^{\text{ioniz}}(p,t) = \widetilde{T}(\widetilde{P})_{lm}(p,t) - \sum_n a_{nlm}^{T(P)}(t)F_{nl}(p). \quad (6)$$

The positive energy component of the wave function, $\Phi_{\text{ioniz}}(\vec{p},t)$, is constructed by substituting the $\widetilde{T}(\widetilde{P})_{lm}^{\text{ioniz}}$ in place of $\widetilde{T}(\widetilde{P})_{lm}$ in Eq. (2), and the individual target and projectile positive energy components are referred to as Φ_{ioniz}^T and Φ_{ioniz}^P, respectively. The validity of this subtraction relies on an accurate calculation of the total wave function and the assumption that $a^{T(P)}(t)$ have reached the asymptotic values. Since the time-dependent wave function is not a stationary state, there is no reason *a priori* to expect $\Phi_{\text{ioniz}}(\vec{p},t)$ to become time independent for large internuclear separation. Thus it is not immediately clear how one extracts the experimentally observed ejected-electron spectra. We will return to this point later.

C. Parameters of the TCMSD calculation

Before presenting the TCMSD results we discuss the actual parameters used in the calculation. Selection of the proper radial grid on which the B splines are defined and a suitable number of harmonics about each proton is critical for a valid calculation. In addition, an appropriate set of fitting points must be chosen, avoiding linear dependence difficulties within the basis set. Although the basis set can be predetermined, to some extent, by physical reasoning, there was some experimentation involved in finding the optimum choice. The same basis set was used for all impact energies in this work.

Since the two-center nature of the ion-atom collision is taken into account already by the expansion about each nucleus, much of the numerical effort goes toward solving for the radial functions. An important generalization of the

present work over Ref. [25] was to allow p_{max}, the radial momentum where the asymptotic form takes over from the B- spline representation, to vary with the angular momentum quantum number l. One expects larger momentum to be important for lower l, since low l partial waves extend to smaller r in configuration space, where the kinetic energy is larger. Three partial waves are taken about each proton with $p_{\text{max}}^{l=0}=4.0$ a.u., $p_{\text{max}}^{l=1}=2.5$ a.u., and $p_{\text{max}}^{l=2}=2.5$ a.u. Since the quantization axis is chosen to be perpendicular to the collision plane, the odd-parity states are never populated due to the even parity of the initial s state. Thus six spherical harmonics cover all partial waves up to and including $l=2$. It was found empirically that a radial grid with spacing 0.05 a.u. was necessary to propagate the electron wave function to $vt=40$ a.u. past the point of closest approach. The current program allows for nonuniform grid spacing; however, this flexibility does not aid in representing the radial functions with fewer B splines. A uniform grid supplied the ''best'' calculations; a point we return to in the discussion.

All calculations were started with the projectile at $vt = -20$ a.u. The end point of the calculation depended on the impact energy. For the 5 keV collision integration to $vt = 25$ a.u. was stable with present calculational parameters, while the 25 keV collision could be integrated to $vt = 40$ a.u. The reason for this is discussed in the next section. These distances are by no means large enough to establish the asymptotic electron wave function; however, as will be seen, the main features of the collision are determined early on.

III. RESULTS AND DISCUSSION

From the solution of the time-dependent Schrödinger equation we first discuss interesting features of the total wave function and then go on to describe the component that represents ionization in order to extract the collision plane momentum distribution of the ejected-electrons. The time dependence of the ejected electron cloud is studied at large internuclear separations in order to estimate the momentum distribution of the ejected-electron as the two nuclei reach infinite internuclear separation. Finally, the behavior of the electron momentum distribution versus projectile impact energy is examined.

A. The total wave function

Figure 1 shows a slice of the electron wave function amplitude on the collision plane at $vt=19.2$ a.u. in both (a) momentum space and (b) configuration space, for a projectile with velocity of 1.0 a.u. and impact parameter of 1.2 a.u. To bring out weaker features of the wave function we plot the amplitude instead of the probability density. In Fig. 1(b) the configuration space wave function is concentrated on the two centers, reflecting that elastic scattering and electron capture to the $1s$ state are the main features of the collision. The ionization component is a large part of the amplitude far away from both nuclear centers, spreading out further as the projectile recedes. On the other hand, in momentum space the distribution of the whole wave function remains well localized, but as can be seen in Fig. 1(a) conspicuous interference fringes appear. The origin of the straight and nearly
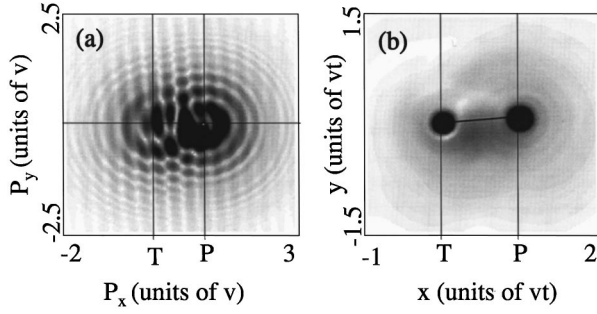
FIG. 1. (a) Contour plot of the amplitude of the total electron wave function in momentum space for a proton on hydrogen collision, impact parameter $b = 1.2$ a.u., projectile velocity $v = 1.0$ a.u., and internuclear separation $vt = 19.2$ a.u. The cut is taken for momenta lying in the collision plane. (b) Corresponding contour plot of the electron wave function amplitude in configuration space.

vertical fringes is interference between electron distribution about target and projectile centers. The number of fringes is proportional to the physical separation between the two protons as is the case with the two-slit experiment. The phase factor responsible for the straight fringes in Fig. 1(a) has been anticipated, and it is included in the plane-wave phase factor in the expansion Eq. (2). The circular fringes, however, are not built into the wave function ansatz explicitly; they appear in the numerical solution of the radial functions. They force us to adopt a uniform and fine grid to represent the momentum-space radial functions.

A recent study by Illescas and Riera [30] explains the origin of the circular fringes. Reference [30] demonstrates that the primary motion of ejected electrons in an ion-atom collision is a ''free expansion'' away from the collision center and that the expansion can be accounted for by including the phase factor $\exp[ivr^2/(2R)]$ in the expression of the *total* electron wave function in configuration space. The same phase factor was introduced by Soloviev and Vinitsky [31] in developing ion-atom collision theory in scaled space. The explosion phase factor oscillates more rapidly with increasing r, reflecting the fact that further components of the electron density are moving faster much like a Hubble expansion. Transforming the explosion factor to momentum space, one obtains a convolution of the momentum-space wave function with the phase factor $\exp[-iRp^2/(2v)]$ [32]. The new explosion factor is similar to the configuration space form; the differences are the sign and the interchange of the roles of the internuclear separation R and the projectile speed v. The effect of the explosion factor on the ejected-electron component is different than the effect on the bound component, because the ejected component is expanding in configuration space while the bound component is not. And in momentum space the ejected component and bound components of the wave function overlap, resulting in the circular interference fringes [32]. The fact that the lower energy calculations became unreliable at lower values of internuclear separation R is now clear. The projectile velocity enters in the denominator of the momentum-space explosion factor, resulting in more rapid oscillations for the same R.

B. Time evolution of ejected-electron distribution

We focus next on the ionization channel for a $p + H$ collision with $v = 1$ a.u. and $b = 1.2$ a.u. First in Fig. 2(a) and
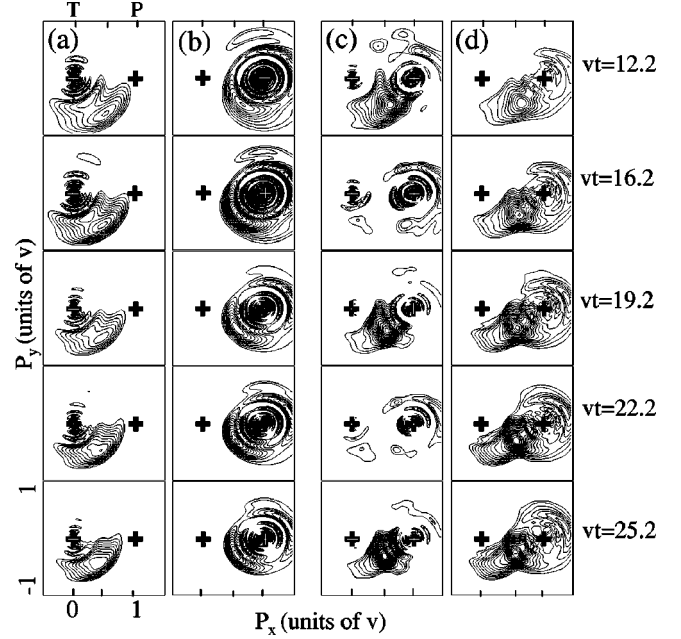

FIG. 2. Time evolution of the positive energy component of the momentum-space probability density in the collision plane for 25-keV ($v = 1$ a.u.) protons on hydrogen at impact parameter $b = 1.2$ a.u. (a) Positive energy target density $|\Phi_{ioniz}^T|^2$. (b) Positive energy projectile density $|\Phi_{ioniz}^P|^2$. (c) Total positive energy probability density $|\Phi_{ioniz}|^2 = |\Phi_{ioniz}^T + \exp[-i(\vec{p} \cdot \vec{R} - \frac{1}{2}v^2 t)]\Phi_{ioniz}^P|^2$. (d) Probability density from an incoherent superposition of target and projectile positive energy expansions $|\Phi_{ioniz}^T|^2 + |\Phi_{ioniz}^P|^2$, integrated over p_z. The crosses indicate the position of both target and projectile protons in velocity space.

Fig. 2(b) we show the probability density of the ionization component on the collision plane about the target and the projectile centers, respectively. The shape of the distribution about each center does not change much as vt is increased. One clear feature is that the transverse momentum distribution associated with the target center points mostly in the $-y$ direction and as the time increases, the distribution shrinks toward the target nucleus. On the projectile center, the transverse momentum is more evenly distributed with respect to the $+y$ and $-y$ sides, and compression toward the projectile nucleus is also observed as the time is increased.

The complete ionization probability density, which is obtained from the coherent sum of the positive energy wave functions from the two centers, is shown in Fig. 2(c). Due to two-center interference the ionization probability density oscillates rapidly with time (the time frames were chosen to show the extrema of the oscillation). Interestingly, the vertical fringes, which are seen in the total wave function in momentum space, Fig. 1(a), are not seen when the bound states on both centers are subtracted out. As stated earlier, the interference of bound states on both nuclei is analogous to a two-slit experiment, since in configuration space bound states are localized about their respective centers. Electron probability density, corresponding to ionization, is very diffuse in configuration space. The ejected-electron distribution forms a broad distribution encompassing both nuclei in configuration space. Thus Fourier transformation to momentum space of the ionization component is more analogous to the single-slit experiment and one sees no rapid interference

fringes in the component of momentum parallel to the internuclear axis.

The time oscillation in Fig. 2(c) is too fast to be seen experimentally, thus we show the incoherent superposition of the densities on the two centers. To a good approximation this is equivalent to a time averaging over one cycle of the time oscillation. The distributions shown in Fig. 2(d) are an incoherent sum of the positive energy component of the target and projectile expansions. Moreover, the momentum component perpendicular to the collision plane, p_z, is integrated over since this is also what is done in experiment, see, e.g., [19]. The time evolution shown in Fig. 2(d) is more gradual than what appears in Fig. 2(c). As time increases one notices a compression of the ejected-electron cloud in transverse momentum and stretching in longitudinal momentum. This is a consequence of the long range Coulomb forces from the two receding protons. Since the calculation stops, in this case, at $vt = 40$ a.u. (recall that $p + $H collisions at 25 keV could be integrated to larger internuclear separation than 5 keV), there is some question as to what the effect of the Coulomb interaction is for larger distances. For example, does the peak move from negative to positive transverse momentum? A classical model calculation of the peak in momentum space indicates that the electron flow remains at negative transverse momentum p_y. Since the ejected-electron distribution for the collision shown in Fig. 2 shows a single peak in both configuration space and momentum space, one can assign their respective maxima to an initial position and momentum for a representative classical calculation. The results show that the ejected-electron momentum remains in the negative y direction, and this result is largely independent of the starting position. Note this argument does not apply for distributions with multiple maxima. But examining the ejected-electron distribution for other impact energies also shows only an overall transverse compression and longitudinal spreading of the ionization pattern which is determined early on. Typically, the basic pattern of ejected electrons is determined when the projectile is 10 to 12 a.u. past closest approach.

C. Dependence of ejected-electron distribution on collision velocity

In this subsection we present the electron momentum distribution for proton on hydrogen collisions at a fixed impact parameter $b = 1.2$ a.u. for energies ranging from 5 to 100 keV. The results are shown in Fig. 3. To compare ionization for different velocities, we choose a fixed point after the collision: $vt = 24.2$ a.u. On each frame, we show the ejected-electron momentum probability distribution projected onto the collision plane, the transverse distribution by integrating over p_x, and the longitudinal distribution by integrating over p_y.

There are two general features that deserve special mention. (1) In the longitudinal direction, the electron momentum tends to lie between 0 and v, the projectile velocity. In fact, the longitudinal momentum distributions all have peaks near $v/2$ except at the highest collision energy 100 keV shown in Fig. 3(f), where the ejected electron is centered near the target as expected for collisions much above the matching velocity. (2) The transverse momentum distribu-
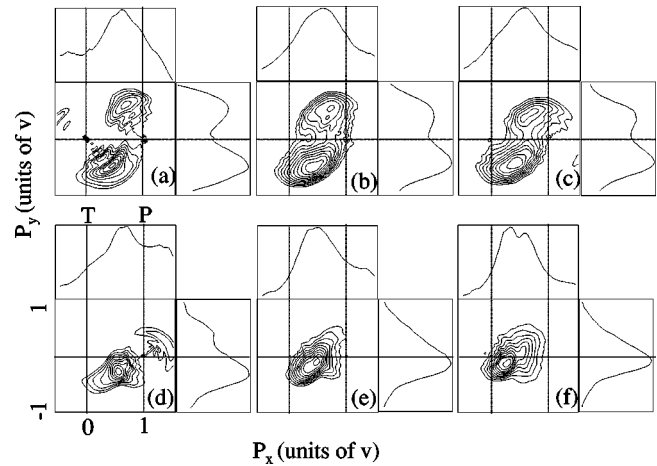

FIG. 3. Ejected-electron distributions projected onto the collision plane for proton on hydrogen collisions at impact parameter $b = 1.2$ a.u. for projectile energies ranging from 5 keV to 100 keV. Next to each distribution is a plot showing only the transverse momentum distribution after integrating out the longitudinal momentum, and above each distribution is a plot showing only the longitudinal momentum distribution after integrating out the transverse momentum. All frames are for $vt = 24.2$ a.u. (a) 5 keV; (b) 10 keV; (c) 15 keV; (d) 25 keV; (e) 50 keV; (f) 100 keV.

tion of the electron shows two peaks at lower energies from 5 to 15 keV. At higher energies the two peaks coalesce into a single peak, with the peak occurring at negative p_y.

How do the present results compare to existing experimental data and other theoretical calculations? There are no COLTRIMS measurements of electron momentum distributions on the proton-hydrogen system so far. For protons colliding with He in the 5–15 keV region, measurements by Dörner *et al.* [18] indeed showed the two-peak structure similar to Figs. 3(a)–3(c), however, with one major difference. The experimental data show rapid oscillation between the two peaks as the collision energy is varied from 5 to 15 keV, while for our calculations on the proton-hydrogen system the two peaks maintain nearly the same relative height without any visible oscillation in the same energy range. Other energies between 5, 10, and 15 keV, not shown here, were also checked. The experiment measures the ejected-electron distribution for a range of projectile impact parameters, but Ref. [18] shows that only the detailed shape of the jet structure changes with impact parameter and the gross asymmetry features vary little with impact parameter. On the other hand, the two collision systems are not expected to behave similarly at low energies. For the symmetric proton-hydrogen atom collision system, the united atom $2p\sigma$-$2p\pi$ rotational coupling is essential for promotion of the electron to the excited states as well as to the continuum. Our results in Figs. 3(a)–3(c) reflect that the ejected electron retains most of this π character. For proton-helium collisions in the same energy range, the radial coupling between the two lowest σ molecular states is essential for the promotion of the electron to the excited states and thus to the continuum states as well. In this energy region there is experimental evidence [33] that the π and the σ components of the electron are of nearly equal importance since the integrated alignment parameter A_{20} for electron capture to H($2p$) states changes sign in the 5–15 keV region. We mention that A_{20} is a mea-
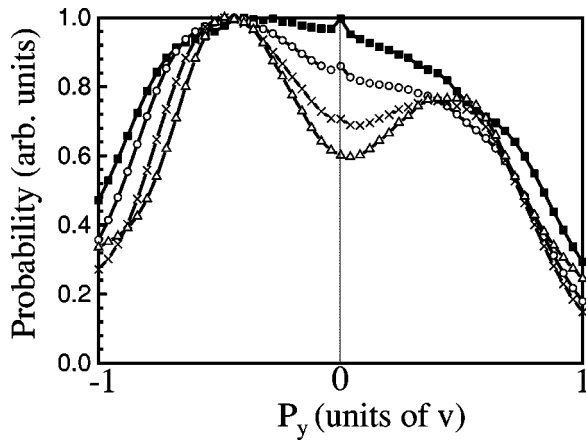
FIG. 4. Time evolution of the ejected-electron transverse momentum distribution for a 10 keV $p+$H collision at impact parameter $b=1.2$ a.u. The momentum components perpendicular to the collision plane p_z and parallel to the incoming projectile p_x have been integrated over. The four curves represent the distribution at different internuclear distances: $vt=14.2$, 19.2, 24.2, and 29.2 a.u., seen from top to bottom along the $p_y=0$ line. All curves have their maximum value normalized to unity.

sure of the relative magnitude between the atomic $2p\sigma$ and $2p\pi$ states and that the quantization axis used in the discussion in this subsection refers to the internuclear axis. Thus we speculate that the rapid oscillation of the transverse electron momentum distribution for the proton-helium system is not a general feature of ion-atom collisions at low energies, but is specific to this system. In fact, measurements by Abdallah *et al.* [19,20] show that the momentum distributions vary significantly for various singly charged projectiles incident on He and Ne targets. Interestingly, for the symmetric He$^+$ on He system the momentum distribution behaves similarly to our prediction for the proton on hydrogen system in that no rapid oscillation of the transverse momentum occurs [21], even though the momentum distribution itself is asymmetric to the opposite side of the $p+$H case.

The only other theoretical approach which gives the momentum distribution of the ejected electrons is the Sturmian two-state theory of Macek and Ovchinnikov [24]. They considered the ionization via T promotion [23] which is essentially ionization by the saddle-point mechanism. By extracting the σ and π amplitudes from hidden crossing theory [16], they derive a two-state model where the fast oscillation of the transverse electron momentum is attributed to interference from the coherent sum of the two amplitudes. In Ref. [24] the theory of Macek and Ovchinnikov reported the rapid oscillation for a proton-hydrogen system at the same projectile energies as the oscillation observed for the proton-helium system [18]. We do not see the oscillation in the 5–15 keV region, see Figs. 3(a)–3(c). Instead, examining Figs. 3(c) and 3(d), one sees a rapid shift in the transverse momentum distribution, near the saddle velocity, in the 15–25 keV region.

The time evolution of the asymmetry in the transverse momentum distribution of ejected electrons is checked to see if the asymmetry, seen for $R=24.2$, can be expected to persist. To investigate this we have shown in Fig. 4 four time steps, $vt=14.2, 19.2, 24.2$, and 29.2 a.u., of the ejected-electron transverse momentum for the 10 keV collision. One can see sharpening of the double jet structure of the trans-

verse momentum distribution, but there is no evidence of oscillation along the trajectory. Our calculations show that the basic shape of the ejected-electron distribution in momentum space is established early on.

It appears that there is another discrepancy in the direction of the transverse momentum when one looks at the bottom of Fig. 1 in Ref. [24] and compares with the 15 keV result of Fig. 3(c). However, these results are not inconsistent. The coordinates $k_\perp$ and $k_\parallel$ in Ref. [24] refer to components of the momentum parallel and perpendicular to the internuclear axis. So the sign relative to the projectile impact parameter is indeterminate, while in Fig. 3 the sign of p_y tells whether the electron momentum is parallel or antiparallel to the projectile impact parameter vector.

IV. THE ROLE OF THE SADDLE-POINT MECHANISM

In the original triple-center close-coupling calculation of Winter and Lin [12] it was found that there was significant probability for ionization left at the midpoint of the internuclear line for proton collisions with atomic hydrogen in the low energies (roughly below 15 keV). Winter and Lin argued, in analogy with the Wannier theory of electron impact ionization [34], that ionization probability accumulates at the potential saddle. This close-coupling calculation, however, was unable to provide any information about the ejected-electron momentum distribution. Since the saddle is moving at velocity $v/2$ in the laboratory frame, it was speculated that observation of enhancement of electrons at velocity $v/2$ is a manifestation of the saddle-point mechanism for ionization. In the meanwhile early classical Monte Carlo trajectory calculations [1] indicated that the doubly differential cross sections indeed show a discernible peak at $v/2$, and saddle-point electrons were taken to be synonymous with $v/2$ electrons for symmetric systems.

In the last two decades there have been numerous experiments aiming at observing clear features of the ejected-electron momentum near $v/2$, or in general, the structure near the velocity of the saddle point for a given collision system. There are two issues. The first is whether there are discernible features for the electron momentum near the saddle-point velocity, the second issue is whether a peak of the ejected-electron distribution at $v/2$ can be attributed to the saddle-point mechanism, akin to Wannier theory.

At projectile velocities above the matching velocity experimentalists do not agree on the first issue. While there are groups presenting evidence of the existence of the $v/2$ electrons [2–6], there are other groups disputing the evidence [7–11]. It was argued that the "evidence" of the peak structure near the saddle point depends on how the doubly differential cross sections are presented. Nevertheless, all these experiments were carried out at high velocities. Even if there are any features near the saddle-point velocity, they cannot be attributed to the saddle-point mechanism for ionization for such high projectile energies. This was demonstrated experimentally by Abdallah *et al.* [35], where they performed ion-atom collisions with He and Ne target atoms at a fixed projectile velocity of $v=1.63$ a.u. varying only the projectile charge state. Indeed, the distributions for the proton impact show a peak at $v/2$, the saddle point, but increasing the projectile charge state causes the ejected-electron distribution to move toward the projectile center in velocity space. The
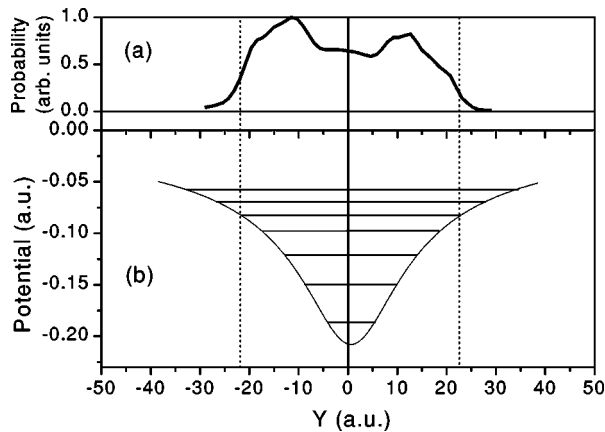
FIG. 5. (a) A transverse slice through the saddle point of the ejected-electron distribution in configuration space. The probability density of the electron comes from a 10-keV collision at impact parameter $b=1.2$ a.u. and internuclear separation of $vt=19.2$ a.u. (b) The potential in the collision plane along y going through the saddle. The horizontal lines represent eigenenergies of the transverse potential, assuming a stationary potential and no motion in the x and z directions. The vertical dotted lines represent estimated turning points based on the shape of the transverse probability distribution.

saddle-point velocity moves instead toward the target center. From the triple-center close-coupling calculations for $p+$H [12] it was concluded that ionization probabilities at the saddle point become negligible for collisions above 15 keV yet the longitudinal momentum in the 25–50 keV region, Figs. 3(c) and 3(d) still show a peak at $v/2$. This is clear evidence that it is not always correct to associate electron emission at $v/2$ (or the saddle-point velocity) with the saddle-point mechanism for ionization.

To our knowledge the only experiment for proton on hydrogen collisions that tests the saddle-point mechanism is the experiment of Pieksma et al. [17]. They searched for features near $v/2$, but, as we stated earlier, this feature is not sufficient proof of the saddle-point mechanism. With theory by Pieksma and Ovchinnikov [16], Ovchinnikov and Macek [22], Macek and Ovchinnikov [24], and COLTRIMS experiments by Dörner et al. [18] and Abdallah et al. [19] the picture of the saddle-point mechanism is more well defined. In the hidden crossings picture the saddle-point mechanism is represented by a series of branch points labeled the T series. In fact, if the saddle-point mechanism is to play an important role, it is desirable to examine the transverse momentum distribution. Since the electron can reach quasistability near the saddle only if its motion is perpendicular to the internuclear line, a manifestation of the saddle-point mechanism is that the transverse probability distribution should show structure. Since the complete wave function is available with the present calculation, we can examine the ionization component in configuration space and compare the extent of the ejected-electron distribution in the y direction with the binding potential in the transverse direction at the saddle point. Such a comparison gives an idea of the number of transverse modes involved in describing ionization by the saddle-point mechanism. In Fig. 5 we show a transverse cut, along y, of the configuration space ejected-electron distribution, projected onto the collision plane, at the saddle point for a 10

keV $p+$H collision at an internuclear separation of $R=19.2$ a.u. Along with the transverse distribution, the binding potential at the saddle is plotted with the energy of the adiabatic transverse modes indicated by horizontal lines. The asymmetric π structure anticipated in Ref. [24] appears, but from the extent of the transverse probability distribution it is clear that the ejected-electron distribution is a coherent excitation of many transverse modes centering on the fifth state. The fact that the simple π structure appears reflects the importance of rotational coupling from the initial σ state and the fact that the π structure survives, despite the many transverse modes that comprise it, results from the rapidity of the collision. Since excitation to higher transverse modes, where the binding is weaker than the harmonic oscillator potential, is important, it is understandable that no oscillation of the transverse momentum distribution is seen in Fig. 4.

V. CONCLUSION

The two-center momentum-space discretization method is primarily a numerical method for solving the time-dependent Schrödinger equation. It does, however, allow for inclusion of basic physical aspects which increase understanding of the system and reduce the computational effort. Calculating in momentum space allows the containment of both bound and free components of the wave function in a finite volume. For the proton-hydrogen collision system the two-center nature of the problem introduces oscillatory structure in momentum space and in time. We account for both effects with a two-center expansion and a plane-wave factor. Taking into account the gross physical features of the ion-atom collision allows for accurate integration of the Schrödinger equation, revealing detailed information on weak processes such as ionization.

We have shown the ejected-electron distributions for $p+$H collisions with projectile energies ranging from 5 to 100 keV and impact parameter $b=1.2$ a.u. At the low velocity we find the forked distribution seen in experiment [18–20] and shown in theory [22–24]. The ejected-electron distribution shows little dependence on projectile velocity until the projectile energy passes 15 keV, where the forked structure fades, replaced by a single peak at negative transverse momentum (antiparallel with the impact parameter vector). Our calculation shows that electron density entering the saddle region populates many transverse modes coherently. The coherence maintains the simple π structure, and the spectrum of states involved gives a gradual dependence of the ejected-electron cloud for projectile energies from 5 to 15 keV. The fact that many states on the potential saddle are populated and that the basic shape of the ejected-electron cloud is established at small internuclear separation $R<10$ a.u. is consistent with the experimental finding that the particular shape of the ejected-electron distribution is system dependent [18–20].

[1] R.E. Olson, Phys. Rev. A **27**, 1871 (1983).

[2] W. Meckbach, P.J. Focke, A.R. Goni, S. Suárez, J. Macek, and M.G. Menendez, Phys. Rev. Lett. **57**, 1587 (1986).

[3] R.E. Olson, T.J. Gay, H.G. Berry, E.B. Hale, and V.B. Irby, Phys. Rev. Lett. **59**, 36 (1987).

[4] V.D. Irby, T.J. Gay, J.W. Edwards, E.B. Hale, M.L. McKenzie, and R.E. Olson, Phys. Rev. A **37**, 3612 (1988).

[5] T.J. Gay, M.W. Gealy, and M.E. Rudd, J. Phys. B **23**, L823 (1990).

[6] V.D. Irby, S. Datz, P.F. Ditmer, N.L. Jones, H.F. Krause, and C.R. Vane, Phys. Rev. A **47**, 2957 (1993).

[7] G. Bernardi *et al.*, Phys. Rev. A **40**, 6863 (1989).

[8] G. Bernardi, P. Fainstain, C.R. Garibotti, and S. Suárez, J. Phys. B **23**, L139 (1990).

[9] W. Meckbach, S. Suárez, P. Focke, and G. Bernardi, J. Phys. B **24**, 3763 (1991).

[10] S. Suárez *et al.*, Phys. Rev. A **48**, 4339 (1993).

[11] R.D. DuBois, Phys. Rev. A **48**, 1123 (1993); **50**, 364 (1994).

[12] T.G. Winter and C.D. Lin, Phys. Rev. A **29**, 3071 (1984).

[13] T.G. Winter, Phys. Rev. A **37**, 4656 (1988).

[14] B.M. McLaughlin, T.G. Winter, and J.F. McCann, J. Phys. B **30**, 1043 (1997).

[15] L.F. Errea, C. Harel, C. Illescas, H. Jouin, L. Méndez, B. Pons, and A. Riera, J. Phys. B **31**, 3199 (1998).

[16] M. Pieksma and S.Y. Ovchinnikov, J. Phys. B **27**, 4573 (1994).

[17] M. Pieksma, S.Y. Ovchinnikov, J. van Eck, W.B. Westerveld, and A. Niehaus, Phys. Rev. Lett. **73**, 46 (1994).

[18] R. Dörner, H. Khemliche, M.H. Prior, C.L. Cocke, J.A. Gary, R.E. Olson, V. Mergel, J. Ullrich, and H. Schmidt-Böcking, Phys. Rev. Lett. **77**, 4520 (1996).

[19] M.A. Abdallah, C.L. Cocke, W. Wolff, H. Wolf, S.D. Kravis, M. Stöckli, and E. Kamber, Phys. Rev. Lett. **81**, 3627 (1998).

[20] M.A. Abdallah, W. Wolff, H. Wolf, C.L. Cocke, and M. Stöckli, Phys. Rev. A **58**, R3379 (1998).

[21] M. A. Abdallah, Ph.D. thesis, Kansas State University, 1997.

[22] S.Y. Ovchinnikov and J.H. Macek, Phys. Rev. Lett. **75**, 2474 (1995).

[23] S.Y. Ovchinnikov, J.H. Macek, and D.B. Khrebtukov, Phys. Rev. A **56**, 2872 (1997).

[24] J.H. Macek and S.Y. Ovchinnikov, Phys. Rev. Lett. **80**, 2298 (1998).

[25] E.Y. Sidky and C.D. Lin, J. Phys. B **31**, 2949 (1998).

[26] K. Momberger, A. Belkacem, and A. H. Sørensen, Phys. Rev. A **53**, 1605 (1996).

[27] J.C. Wells, D.R. Schultz, P. Gavras, and M.S. Pindzola, Phys. Rev. A **54**, 593 (1996).

[28] D.R. Schultz, J.C. Wells, P.S. Kristić, and C.O. Reinhold, Phys. Rev. A **56**, 3710 (1997).

[29] A. Kolakowska, M.S. Pindzola, F. Robicheaux, D.R. Schultz, and J.C. Wells, Phys. Rev. A **58**, 2872 (1998).

[30] C. Illescas and A. Riera, Phys. Rev. Lett. **80**, 3029 (1998); **81**, 1350 (1998).

[31] E.A. Soloviev and S.I. Vinitsky, J. Phys. B **27**, L557 (1985).

[32] E. Y. Sidky, in *Applications of Accelerators in Research and Industry*, Proceedings of the Fifteenth International Conference, Denton, Texas, edited by J. L. Duggan and J. L. Morgan (University of North Texas, Denton, 1999).

[33] R. Hippler, W. Harbich, M. Faust, H.O. Lutz, and L.J. Dubé J. Phys. B **19**, 1507 (1986).

[34] G.H. Wannier, Phys. Rev. **90**, 817 (1953).

[35] M.A. Abdallah, S. Kravis, C.L. Cocke, Y. Wang, V.D. Rodriguez, and M. Stöckli, Phys. Rev. A **56**, 2000 (1997).